

April 15, 2019

# Cross-Correlation of the Cosmic Microwave Background with the 2MASS Galaxy Survey: Signatures of Dark Energy, Hot Gas, and Point Sources

Niayesh Afshordi,\* Yeong-Shang Loh, and Michael A. Strauss

*Princeton University Observatory, Princeton, NJ 08544, USA*

## Abstract

We cross-correlate the Cosmic Microwave Background (CMB) temperature anisotropies observed by the Wilkinson Microwave Anisotropy Probe (WMAP) with the projected distribution of extended sources in the Two Micron All Sky Survey (2MASS). By modelling the theoretical expectation for this signal, we extract the signatures of dark energy (Integrated Sachs-Wolfe effect;ISW), hot gas (thermal Sunyaev-Zeldovich effect;thermal SZ), and microwave point sources in the cross-correlation. Our strongest signal is the thermal SZ, at the  $3.1 - 3.7\sigma$  level, which is at least 40% ( $2\sigma$ ) smaller than the theoretical prediction. We also see the ISW signal at the  $2.5\sigma$  level, which is consistent with the expected value for the concordance  $\Lambda$ CDM cosmology, and is an independent signature of the presence of dark energy in the universe. Finally, we see a signature for the microwave point sources at the  $2.7\sigma$  level.

PACS numbers: 98.65., 98.65.Dx, 98.65.Hb, 98.70.Dk, 98.70.Vc, 98.80., 98.80.Es

---

\*Electronic address: afshordi@astro.princeton.edu

## I. INTRODUCTION

The recently released WMAP [5] results constrain our cosmology with an unprecedented accuracy. Most of these constraints come from the linear fossils of the early universe which have been preserved in the temperature anisotropies of the CMB. These are the ones that can be easily understood and dealt with, within the framework of linear perturbation theory. However, there are also imprints of the late universe which could be seen in the WMAP results. Most notably, the measurement of the optical depth to the surface of last scattering,  $\tau \simeq 0.17$ , which implied an early reionization of the universe, was the biggest surprise. There is also the strangely small amplitude of the large-angle CMB anisotropies which remains unexplained[47].

Can we extract more about the late universe from WMAP? Various secondary effects have been studied in the literature (see e.g.[23] which lists a few). The main secondary anisotropy at large angles is the so-called Integrated Sachs-Wolfe (ISW) effect[41], which is a signature of the decay of the gravitational potential at large scales. This could be either a result of spatial curvature, or presence of a component with negative pressure, the so-called dark energy, in the universe[38]. Since WMAP has constrained the deviation from flatness to less than 4%, the ISW effect may be interpreted as a signature of dark energy. At smaller angles, the dominant source of secondary anisotropy is the thermal Sunyaev-Zeldovich (SZ) effect[51], which is due to scattering of CMB photons by hot gas in the universe.

However, none of these effects can make a significant contribution to the CMB power spectrum below  $\ell \sim 1000$ , and thus they are undetectable by WMAP alone. One possible avenue is cross-correlating CMB anisotropies with a tracer of the density in the late universe[11, 13, 39]. This was first done by [8] who cross-correlated the COBE/DMR map[4] with the NRAO VLA Sky Survey (NVSS)[10]. After the release of WMAP, different groups cross-correlated the WMAP temperature maps with various tracers of the low-redshift universe. This was first done with the ROSAT X-ray map in [14], where a non-detection of the thermal SZ effect puts a constraint on the hot gas content of the universe. [36] looked at the cross-correlation with the NVSS radio galaxy survey, while [9] repeated the exercise for NVSS, as well as the HEAO-1 hard X-ray background survey, both of which trace the universe around redshift of  $\sim 1$ . Both groups found their result to be consistent with the expected ISW signal for the WMAP concordance cosmology [5], i.e. a flat  $\Lambda$ CDM universe

with  $\Omega_m \simeq 0.3$ , at the  $2 - 3\sigma$  level. Their result is consistent with the  $\Lambda$ CDM paradigm which puts most of the energy of the universe in dark energy[38].

More recently, [16] cross-correlated WMAP with the APM galaxy survey[32] which traces the galaxy distribution at  $z \sim 0.15$ . This led to an apparent detection of both the thermal SZ and ISW signals. However, the fact that they use a jack-knife covariance matrix to estimate the strength of their signal, while their jack-knife errors are significantly smaller than those obtained by Monte-Carlo realizations of the CMB sky (compare their Figure 2 and Figure 3) weakens the significance of their claim. Indeed, as we argue below (see III.C), using Monte-Carlo realizations of the CMB sky is the only reliable way to estimate a covariance matrix if the survey does not cover the whole sky.

[34] cross-correlates the highest frequency band (W-band) of the WMAP with the ACO cluster survey[1], as well as the galaxy groups and clusters in the APM galaxy survey. They claim a  $2.6\sigma$  detection of temperature decrement on angles less than  $0.5^\circ$ , which they associate with the thermal SZ effect. However they only consider the Poisson noise in their cluster distribution as their source of error. This underestimates the error due to large spatial correlations (or cosmic variance) in the cluster distribution (see III.C). [34] also studies the cross-correlation of the W-band with the NVSS radio sources below a degree and claims a positive correlation at the scale of the W-band resolution. This may imply a possible contamination of the ISW signal detection in [9] and [36]. However the achromatic nature of this correlation makes this unlikely[7].

Finally, [44] and [17] repeated the cross-correlation analysis with the 3400 and 2000 square degrees, respectively, of the Sloan Digital Sky Survey[50]. Both groups claim detection of a positive signal, but they both suffer from the inconsistencies of jack-knife and Monte-Carlo errors.

The 2MASS Extended Source Catalog (XSC)[26] is a full sky, near infrared survey of galaxies whose median redshift is around  $z \sim 0.1$ . The survey has reliable and uniform photometry of about 1 million galaxies, and is complete, at the 90% level for K-magnitudes brighter than 14, over  $\sim 70\%$  of the sky. The large area coverage and number of galaxies makes the 2MASS XSC a good tracer of the ISW and SZ signals in the cross-correlation with the CMB.

In this paper, we study the cross-correlation of the WMAP Q,V and W bands with four different K-magnitude bins of the 2MASS Extended Source Catalog, and

fit it with a three component model which includes the ISW, thermal SZ effects and microwave sources. We compare our findings with the theoretical expectations from the WMAP+CBI+ACBAR+2dF+Ly- $\alpha$  best fit cosmological model (WMAP concordance model from here on; see Table 3 in [5]), which is a flat universe with,  $\Omega_m = 0.27$ ,  $\Omega_b = 0.044$ ,  $h = 0.71$ , and  $\sigma_8 = 0.84$ . We also assume their values of  $n_s = 0.93$ , and  $dn_s/d\ln k = -0.031$  for the spectral index and its running at  $k = 0.05$  Mpc [47].

We briefly describe the relevant secondary anisotropies of the CMB in Sec. II. Sec. III describes the properties of the cross-correlation of two random fields, projected on the sky. Sec. IV summarizes the relevant information on the WMAP temperature maps and the 2MASS Extended Source Catalog. Sec. V describes our results and possible systematics, and Sec. VI concludes the paper.

## II. WHAT ARE THE SECONDARY ANISOTROPIES?

The dominant nature of the Cosmic Microwave Background (CMB) fluctuations, at angles larger than  $\sim 0.1$  degree, is primordial, which makes CMB a snapshot of the universe at radiation-matter decoupling, around redshift of  $\sim 1000$ . However, a small part of these fluctuations can be generated as the photons travel through the low redshift universe. These are the so-called secondary anisotropies. In this section, we go through the three effects which should dominate the WMAP/2MASS cross-correlation.

### A. Integrated Sachs-Wolfe effect

The first one is the Integrated Sachs-Wolfe (ISW) effect[41] which is caused by the time variation in the cosmic gravitational potential,  $\Phi$ . For a flat universe, the anisotropy due to the ISW effect is an integral over the conformal time  $\eta$

$$\delta_{\text{ISW}}(\hat{\mathbf{n}}) = 2 \int \Phi'[(\eta_0 - \eta)\hat{\mathbf{n}}, \eta] d\eta, \quad (1)$$

where  $\Phi' \equiv \partial\Phi/\partial\eta$ , and  $\hat{\mathbf{n}}$  is unit vector in the line of sight. The linear metric is assumed to be

$$ds^2 = a^2(\eta) \{ [1 + 2\Phi(\mathbf{x}, \eta)] d\eta^2 - [1 - 2\Phi(\mathbf{x}, \eta)] \mathbf{d}\mathbf{x} \cdot \mathbf{d}\mathbf{x} \}, \quad (2)$$

and  $\eta_0$  is the conformal time at the present.

In a flat universe, the gravitational potential  $\Phi$  is constant for a fixed equation of state and therefore observation of an ISW effect is an indicator of a change in the equation of state of the universe. Assuming that this change is due to an extra component in the matter content of the universe, the so-called dark energy, this component should have a negative pressure to become important at late times[38]. Therefore, observation of an ISW effect in a flat universe is a signature of dark energy.

The ISW effect is observed at large angular scales because most of the power in the fluctuations of  $\Phi$  is at large scales. Additionally, the fluctuations at small angles tend to cancel out due to the integration over the line of sight.

## B. Thermal Sunyaev-Zeldovich effect

The other significant source of secondary anisotropies is the so-called thermal Sunyaev-Zeldovich (SZ) effect [51], which is caused by the scattering of CMB photons off the hot electrons of the intra-cluster medium. This secondary anisotropy is frequency dependent, i.e. it cannot be associated with a single change in temperature. If we define a frequency dependent  $T(\nu)$  so that  $I_B[\nu; T(\nu)] = I(\nu)$ , where  $I(\nu)$  is the CMB intensity and  $I_B[\nu; T]$  is the black-body spectrum at temperature  $T$ , the SZ anisotropy takes the form

$$\frac{\delta T(\nu)}{T(\nu)} = -\frac{\sigma_T f(x)}{m_e c} \int \delta p_e[(\eta_0 - \eta) \hat{\mathbf{n}}, \eta] a(\eta) d\eta, \quad (3)$$

where

$$x \equiv h\nu/(k_B T_{\text{CMB}}) \text{ and } f(x) \equiv 4 - x \coth(x/2), \quad (4)$$

and  $p_e$  is the electron pressure. Assuming a linear pressure bias with respect to the matter overdensity  $\delta_m$ :

$$\frac{\delta p_e}{p_e} = b_p \delta_m, \quad (5)$$

Eq.(3) can be written as

$$\delta_{\text{SZ}}(\nu) \equiv \frac{\delta T(\nu)}{T(\nu)} = -F(x) \int \tilde{T}_e \delta_m \frac{H_0 d\eta}{a^2(\eta)}, \quad (6)$$

where

$$\begin{aligned} \tilde{T}_e &= b_p \bar{T}_e, \\ F(x) &= \frac{n_e k_B \sigma_T f(x)}{4 m_e c H_0} = (1.16 \times 10^{-4} \text{keV}^{-1}) \Omega_b h f(x), \end{aligned} \quad (7)$$

and  $\bar{T}_e$  and  $n_e$  are the average temperature and the comoving density of (all) electrons, respectively. In Appendix A, we make an analytic estimate for  $\tilde{T}_e$ , based on the mass function and mass-temperature relation of galaxy clusters.

### C. Microwave Sources

Although technically they are not secondary anisotropies, microwave sources may contribute to the cross-correlation signal, as they are potentially observable by both WMAP and 2MASS. For simplicity, we associate an average microwave luminosity with all 2MASS sources. We can relax this assumption by taking this luminosity to be a free parameter for each magnitude bin, and/or removing the clustering of the point sources. As we discuss in Sec. V.C, neither of these change our results significantly.

For the microwave spectrum in different WMAP frequencies, we try both a steeply falling antenna temperature  $\propto 1/\nu^{2-3}$  (consistent with WMAP point sources[6]) and a Milky Way type spectrum which we obtain from the WMAP observations of the Galactic foreground [6].

In Appendix B, assuming an exponential surface emissivity with a scale length of 5 kpc for the Galactic disk and a small disk thickness, we use the Galactic latitude dependence of the WMAP temperature to determine the luminosity of the Milky Way (Eq.B6) in different WMAP bands:

$$L_Q^* = 1.7 \times 10^{37} \text{ erg s}^{-1},$$

$$L_V^* = 3.0 \times 10^{37} \text{ erg s}^{-1},$$

$$\text{and } L_W^* = 1.0 \times 10^{38} \text{ erg s}^{-1}. \quad (B6)$$

These values are within 50% of the observed WMAP luminosity of the Andromeda galaxy(see Appendix B) [52]. In V.C, we compare the observed average luminosity of the 2MASS sources to these numbers (see Table II).

The contribution to the CMB anisotropy due to Point Sources (see Eq.B2) is given by

$$\delta_{PS}(\hat{\mathbf{n}}) = \frac{\delta T(\hat{\mathbf{n}})}{T} = \frac{4\pi^2 \hbar^3 c^2 \sinh^2(x/2) L(x)}{(x k_B T_{\text{CMB}})^4 \Delta x} \int dr \left( \frac{r}{d_L(r)} \right)^2 n_c(r) \delta_g(r, \hat{\mathbf{n}}), \quad (8)$$

where  $\Delta x$  is the effective bandwidth of the WMAP band[5],  $n_c(r)$  is the average comoving number density of the survey galaxies,  $d_L$  is luminosity distance, and  $\delta_g$  is the galaxy overdensity.

### III. THE CROSS-CORRELATION POWER SPECTRUM

#### A. The Expected Signal

We first develop the theoretical expectation value of the cross-correlation of two random fields, projected on the sky. Let us consider two random fields  $A(\mathbf{x})$  and  $B(\mathbf{x})$  with their Fourier transforms defined as

$$A_{\mathbf{k}} = \int d^3\mathbf{x} e^{-i\mathbf{k}\cdot\mathbf{x}} A(\mathbf{x}), \text{ and } B_{\mathbf{k}} = \int d^3\mathbf{x} e^{-i\mathbf{k}\cdot\mathbf{x}} B(\mathbf{x}). \quad (9)$$

The cross-correlation power spectrum,  $P_{AB}(k)$  is defined by

$$\langle A_{\mathbf{k}_1} B_{\mathbf{k}_2} \rangle = (2\pi)^3 \delta^3(\mathbf{k}_1 - \mathbf{k}_2) P_{AB}(k_1). \quad (10)$$

The projections of  $A$  and  $B$  on the sky are defined using  $F_A$  and  $F_B$  projection kernels

$$\tilde{A}(\hat{\mathbf{n}}) = \int dr F_A(r) A(r\hat{\mathbf{n}}), \text{ and } \tilde{B}(\hat{\mathbf{n}}) = \int dr F_B(r) B(r\hat{\mathbf{n}}). \quad (11)$$

For the secondary temperature anisotropies, these kernels were given in Eqs.1,6 and 8. For the projected galaxy overdensity, this kernel is

$$F_g(r) = \frac{r^2 n_c(r)}{\int dr' r'^2 n_c(r')}. \quad (12)$$

For our treatment, we assume a constant galaxy bias,  $b_g$ , which relates the galaxy fluctuations,  $\delta_g$ , to the overall matter density fluctuations  $\delta_m$ , up to a shot noise  $\delta_p$

$$\delta_g = b_g \delta_m + \delta_p. \quad (13)$$

In this work, we constrain the galaxy bias,  $b_g$ , by comparing the auto-correlation of the galaxies with the expected matter auto-correlation in our cosmological model. Our bias, therefore, is model dependent.

Now, expanding  $\tilde{A}$  and  $\tilde{B}$  in terms of spherical harmonics, the cross-power spectrum,  $C_{AB}(\ell)$  is defined as

$$\begin{aligned} C_{AB}(\ell) &\equiv \langle \tilde{A}_{\ell m} \tilde{B}_{\ell m}^* \rangle \\ &= \int dr_1 dr_2 F_A(r_1) F_B(r_2) \times \\ &\quad \int \frac{d^3\mathbf{k}}{(2\pi)^3} P_{AB}(k) (4\pi)^2 j_\ell(kr_1) j_\ell(kr_2) Y_{\ell m}(\hat{\mathbf{k}}) Y_{\ell m}^*(\hat{\mathbf{k}}) \\ &= \int dr_1 dr_2 F_A(r_1) F_B(r_2) \int \frac{2k^2 dk}{\pi} j_\ell(kr_1) j_\ell(kr_2) P_{AB}(k), \end{aligned} \quad (14)$$

where  $j_\ell$ 's are the spherical Bessel functions of rank  $\ell$  and  $Y_{\ell m}$ 's are the spherical harmonics.

To proceed further, we use the small angle (large  $\ell$ ) approximation for the spherical Bessel functions

$$j_\ell(x) = \sqrt{\frac{\pi}{2\ell+1}} [\delta_{\text{Dirac}}(\ell + \frac{1}{2} - x) + \mathcal{O}(\ell^{-2})], \quad (15)$$

which yields

$$C_{AB}(\ell) = \int \frac{dr}{r^2} F_A(r) F_B(r) P_{AB} \left( \frac{\ell + 1/2}{r} \right) \cdot [1 + \mathcal{O}(\ell^{-2})]. \quad (16)$$

This is the so called Limber equation [31]. As we do not use the quadrupole due to its large Galactic contamination, the smallest value of  $\ell$  that we use is 3. Direct integration of Eq.(15) (for the ISW signal which is dominant for low  $\ell$ 's, see Figure 7) shows that the Limber equation overestimates the cross-power by less than 2-3% at  $\ell = 3$ , which is negligible compared to the minimum cosmic variance error (about 40%, see III.B) at this multipole. Therefore, the Limber equation is an accurate estimator of the theoretical power spectrum.

Now we can substitute the results of Sec. II (Eqs.1, 6, 8 and 12) into Eq.(16) which yields

$$C_{gT}(x, \ell) = \frac{b_g}{\int dr r^2 n_c(r)} \int dr n_c(r) \{ 2P_{\Phi',m} \left( \frac{\ell + 1/2}{r} \right) - \left[ F(x) \tilde{T}_e H_0 (1+z)^2 - \frac{4\pi^2 \hbar^3 c^2 \sinh^2(x/2) b_g L(x)}{(x k_B T_{\text{CMB}})^4 \Delta x (1+z)^2} \right] P \left( \frac{\ell + 1/2}{r} \right) \}, \quad (17)$$

where  $P(k)$  is the matter power spectrum,  $z$  is the redshift, and  $x$  is defined in Eq.(4). The terms in Eq.(17) are the ISW, SZ and Point Source contributions respectively. Since the ISW effect is only important at large scales, the cross-power of the gravitational potential derivative with matter fluctuations can be expressed in terms of the matter power spectrum, using the Poisson equation and linear perturbation theory, and thus we end up with

$$C_{gT}(x, \ell) = \frac{b_g}{\int dr r^2 n_c(r)} \int dr n_c(r) \{ -3H_0^2 \Omega_m \frac{r^2}{(\ell + 1/2)^2} \cdot \frac{g'}{g} (1+z) - F(x) \tilde{T}_e (1+z)^2 + \frac{4\pi^2 \hbar^3 c^2 \sinh^2(x/2) b_g L(x)}{(x k_B T_{\text{CMB}})^4 \Delta x (1+z)^2} \} P \left( \frac{\ell + 1/2}{r} \right), \quad (18)$$

where  $g$  is the linear growth factor of the gravitational potential,  $\Phi$ , and  $g'$  is its derivative with respect to the conformal time. We will fit this model to our data in Sec. V, allowing a free normalization for each term.

Finally, we write the theoretical expectation for the projected galaxy auto-power,  $C_{gg}$ , which we use to find the galaxy bias. Combining Eqs.12,13 and 16, we arrive at

$$C_{gg}(\ell) = \frac{\int dr r^2 n_c^2(r) [b_g^2 \cdot P \left( \frac{\ell + 1/2}{r} \right) + \gamma \cdot n_c^{-1}(r)]}{[\int dr r^2 n_c(r)]^2}, \quad (19)$$

where the  $n_c^{-1}$  term is the power spectrum of the Poisson noise,  $\delta_p$ , while the extra free parameter,  $\gamma$ , is introduced to include the possible corrections to the Poisson noise due to the finite pixel size. In the absence of such corrections  $\gamma = 1$ . In Sec. V, we seek the values of  $b_g$  and  $\gamma$  that best fit our observed auto-power for each galaxy sub-sample.

To include the effects of non-linearities in the galaxy power spectrum, we use the Peacock & Dodds fitting formula [37] for the non-linear matter power spectrum,  $P(k)$ .

## B. Theoretical errors: cosmic variance vs. shot noise

To estimate the expected theoretical error, again for simplicity, we restrict the calculation to the small angle limit. In this limit, the cross-correlation function can be approximated by

$$C_{AB}(\ell) \simeq \frac{4\pi}{\Delta\Omega} \langle \tilde{A}_{\ell m} \tilde{B}_{\ell m}^* \rangle, \quad (20)$$

where  $\Delta\Omega$  is the common solid angle of the patch of the sky covered by observations of both  $\tilde{A}$  and  $\tilde{B}$  [49].

Assuming gaussianity, the standard deviation in  $C_{AB}$ , for a single harmonic mode, is given by

$$\begin{aligned} \Delta C_{AB}^2(\ell) &= \langle C_{AB}^2(\ell) \rangle - \langle C_{AB}(\ell) \rangle^2 \\ &= \Delta\Omega^{-2} [\langle \tilde{A}_{\ell m} \tilde{B}_{\ell m}^* \rangle \langle \tilde{A}_{\ell m} \tilde{B}_{\ell m}^* \rangle + \langle \tilde{A}_{\ell m} \tilde{A}_{\ell m}^* \rangle \langle \tilde{B}_{\ell m} \tilde{B}_{\ell m}^* \rangle] \\ &= C_{AB}^2(\ell) + C_{AA}(\ell)C_{BB}(\ell). \end{aligned} \quad (21)$$

The number of modes available between  $\ell$  and  $\ell + 1$ , in the patch  $\Delta\Omega$ , is

$$\Delta N \simeq \frac{(2\ell + 1)\Delta\Omega}{4\pi}, \quad (22)$$

and so the standard deviation of  $C_{AB}$ , averaged over all these modes is

$$\Delta C_{AB}^2(\ell) \simeq \frac{4\pi}{\Delta\Omega(2\ell + 1)} [C_{AB}^2(\ell) + C_{AA}(\ell)C_{BB}(\ell)]. \quad (23)$$

In fact, since the main part of CMB fluctuations is of primordial origin, the first term in brackets is negligible for the cross-correlation error, so the error in the cross-correlation function, as one may expect, depends on the individual auto-correlations.

We can use the CMBFAST code [45] to calculate the auto-correlation of the CMB temperature fluctuations. Also, the theoretical expectation for the auto-power of the projected galaxy distribution is given by Eq.(19).

The galaxy/CMB auto-power spectra are dominated by Poisson(shot) noise/detector noise at large  $\ell$ 's. Therefore, the measurement of the thermal SZ signal, which becomes important at large  $\ell$ 's, is limited by the number of observed galaxies, as well as the resolution of the CMB detector (the angle at which signal-to-noise ratio for the CMB measurement is of order unity). On the other hand, for the small  $\ell$  portion of the cross-correlation which is relevant for the ISW signal, the error is set by the matter and CMB power spectra and thus, is only limited by cosmic variance. The only way to reduce this error is by observing a larger volume of the universe.

### C. A Note On the Covariance Matrices

We saw in Section III.C that the errors in cross-correlations could be expressed in terms of the theoretical auto-correlation. However, this is not the whole story.

We have a remarkable understanding of the auto-power spectrum of the CMB. However, if one tries to use the frequency information to, say subtract out the microwave sources, the simple temperature auto-power does not give the cross-frequency terms in the covariance matrix. In fact, in the absence of a good model, the only way to constrain these terms is by using the cross-correlation of the bands themselves. Of course, this method is limited by cosmic variance and hence does not give an accurate result at low multipoles. To solve this problem, we use the WMAP concordance model CMB auto-power for  $\ell \leq 13$ . Since there is no frequency-dependent signal at low  $\ell$ 's, we only use the W-band information, which has the lowest Galactic contamination [6], for our first 4  $\ell$ -bins which cover  $3 \leq \ell \leq 13$  (see the end of Sec. III.D for more on our  $\ell$ -space binning).

There is a similar situation for the contaminants of the 2MASS galaxy catalog. Systematic errors in galaxy counts, due to stellar contamination or variable Galactic extinction, as well as observational calibration errors, may introduce additional anisotropies in the galaxy distribution which are not easy to model. Again, the easiest way to include these systematics in the error is by using the auto-correlation of the observed galaxy distribution, which is inaccurate for low multipoles. Unfortunately, this is also where we expect to see possible

Galactic contamination or observational systematics. The best that we can do to solve this problem is to exclude the quadrupole,  $C(2)$ , from our analysis.

At this point, we should point out a misconception about the nature of Monte-Carlo vs. jack-knife error estimates in some previous cross-correlation analyses, specifically [16, 17]. Many authors have used Gaussian Monte-Carlo realizations of the CMB sky to estimate the covariance matrix of their real-space cross-correlation functions[9, 16, 17, 44]. The justification for this method is that, since the first term in Eq.(23) is much smaller than the second term, the error in cross-correlation for any random realization of the maps is almost the same as the true error, and the covariance of the cross-correlation, obtained from many random Gaussian realizations is an excellent estimator of the covariance matrix. We may also obtain error estimates based on random realizations of one of the maps, as long as the observed auto-power is a good approximation of the true auto-power, i.e. the cosmic variance is low, which should be the case for angles smaller than 20 degrees ( $\ell > 10$ ). Of course, at larger angles , as we mentioned above, one is eventually limited by the systematics of the survey and, unless they are understood well enough, since theoretical error estimate is not possible, there will be no better alternative rather than Monte-Carlo error estimates. In fact, contrary to [16, 17], if anything, the presence of cross-correlation makes Monte-Carlo errors a slight underestimate (see Eq.23). On the other hand, there is no rigorous justification for the validity of jack-knife covariance matrices, and the fact that jack-knife errors could be smaller than the Monte-Carlo errors by up to a factor of three [16, 44] implies that they underestimate the error. As we argue below(see Sec. III.D), since we do our analysis in harmonic space and use most of the sky, our  $\ell$ -bins are nearly independent and performing Monte-Carlo's is not necessary. Our covariance matrix is nearly diagonal in  $\ell$ -space and its elements can be obtained using Eq.(23).

#### D. Angular Cross-Power Estimator

The WMAP temperature maps are set in HEALPix format [19], which is an equal area, iso-latitude pixellization of the sky. As a component of the HEALPix package, the FFT based subroutine ‘map2alm’ computes the harmonic transform of any function on the whole sky. However, as we describe in the next section, in order to avoid contamination by Galactic foreground emission in WMAP temperature maps, and contamination by stars and Galactic

extinction in the 2MASS survey, we have to mask out  $\sim 15\%$  of the CMB and  $\sim 30\%$  of the 2MASS sky. Therefore, we cannot obtain the exact values of the multipoles,  $C_\ell$ , and should use an estimator.

We use a quadratic estimator which is based on the assumption that our masks,  $W(\hat{\mathbf{n}})$ , are independent of the data that we try to extract (see [15] for a review of different estimators). The real-space cross-correlation of the masked fields  $\bar{A}(\hat{\mathbf{n}}) = W_A(\hat{\mathbf{n}})\tilde{A}(\hat{\mathbf{n}})$  and  $\bar{B}(\hat{\mathbf{n}}) = W_B(\hat{\mathbf{n}})\tilde{B}(\hat{\mathbf{n}})$  on the sphere is given by

$$\begin{aligned} & \langle \bar{A}(\hat{\mathbf{n}})\bar{B}(\hat{\mathbf{m}}) \rangle \langle \tilde{A}(\hat{\mathbf{n}})\tilde{B}(\hat{\mathbf{m}}) W_A(\hat{\mathbf{n}})W_B(\hat{\mathbf{m}}) \rangle \\ &= \langle \tilde{A}(\hat{\mathbf{n}})\tilde{B}(\hat{\mathbf{m}}) \rangle \langle W_A(\hat{\mathbf{n}})W_B(\hat{\mathbf{m}}) \rangle, \end{aligned} \quad (24)$$

where, in the last step, we used the independence of data and masks, and averaged over all pairs of the same separation. Assuming that  $\langle W_A(\hat{\mathbf{n}})W_B(\hat{\mathbf{m}}) \rangle$  does not vanish for any separation (which will be true if the masked out area is not very large), we can invert this equation and take the Legendre transform to obtain the un-masked multipoles

$$\begin{aligned} C_{\tilde{A}\tilde{B}}(\ell) &= \sum_{\ell'=0}^{\ell_{max}} F_{\ell\ell'} C_{\bar{A}\bar{B}}(\ell'), \text{ where} \\ F_{\ell\ell'} &= (\ell' + \frac{1}{2}) \int \frac{P_\ell(\cos\theta)P_{\ell'}(\cos\theta)}{\langle W_A W_B \rangle(\theta)} d\cos\theta. \end{aligned} \quad (25)$$

In fact this estimator is mathematically identical [53] to the one used by the WMAP team [21], and, within the computational error, should give the same result. The difference is that we do the inversion in real-space, where it is diagonal, and then transform to harmonic space, while they do the inversion directly in harmonic space. Indeed, using our method, we reproduce the WMAP binned multipoles [22] within 5%. However, we believe our method is computationally more transparent and hence more reliable, while the matrix inversion in harmonic space is unstable for small and irregular masks.

Finally, we comment on the correlation among different multipoles in  $\ell$ -space. Masking about 30% of the sky causes about 30% correlation among neighboring multipoles. We bin our multipoles into 13 bins that are logarithmically spaced in  $\ell$  (covering  $3 < \ell < 1000$ ), while excluding the quadrupole due to its large Galactic contamination in both data sets. The highest correlation between neighboring bins is 15% between the first and the second bins ( $C(3)$  and  $(9C(4) + 11C(5))/20$ ). To simplify our calculations, we neglect this correlation, as any correction to our results will be significantly smaller than the cosmic

variance uncertainty(see V.B), i.e. we approximate our covariance matrix as diagonal in  $\ell$ -space.

## IV. DATA

### A. WMAP foreground cleaned temperature maps

We use the first year of the observed CMB sky by WMAP for our analysis [5]. The WMAP experiment observes the microwave sky in 5 frequency bands ranging from 23 to 94 GHz. The detector resolution increases monotonically from 0.88 degree for the lowest frequency band to 0.22 degree for the highest frequency. Due to their low resolution and large Galactic contamination, the two bands with the lowest frequencies, K(23 GHz) and Ka(33 GHz), are mainly used for Galactic foreground subtraction and Galactic mask construction[6], while the three higher frequency bands, which have the highest resolution and lowest foreground contamination, Q(41 GHz), V(61 GHz), and W(94 GHz), are used for CMB anisotropy spectrum analysis. [6] use the Maximum Entropy Method to combine the frequency dependence of 5 WMAP bands with the known distribution of different Galactic components that trace the dominant foregrounds to obtain the foreground contamination in each band. This foreground map is then used to clean the Q, V and W bands for the angular power spectrum analysis. Similarly, we use the cleaned temperature maps of these three bands for our cross-correlation analysis. We also use the same sky mask that they use, the Kp2 mask which masks out 15% of the sky, in order to avoid any remaining Galactic foreground, as well as 208 identified microwave point sources.

### B. 2MASS extended source catalog

We use galaxies from the Near-IR *Two Micron All Sky Survey* [2MASS; 48] as the large-scale structure tracer of the recent universe. Our primary data set is the public full-sky extended source catalog [XSC; 26]. The  $K_s$ -band isophotal magnitude,  $K_{20}$ , is the default flux indicator we use to select the external galaxies for our analysis.  $K_{20}$  is the measured flux inside a circular isophote with surface brightness of 20 mag arcsec $^{-2}$ . The raw magnitudes from the catalog were corrected for Galactic extinction using the IR reddening map of

Schlegel, Finkbeiner & Davis [43]:

$$K_{20} \rightarrow K_{20} - A_K, \quad (26)$$

where  $A_K = R_K E(B - V) = 0.367 \times E(B - V)$  [54]. There are approximately 1.5 million extended sources with corrected  $K_{20} < 14.3$  after removing known artifacts (cc\_flag != 'a' and 'z') and using only sources from a uniform detection threshold (use\_src = 1).

### 1. Completeness and Contamination

We use the standard log N-log S test to determine the completeness limit of the extended source catalog. The top panel of Figure 1 shows the number of galaxies as a function of  $K_{20}$ . The log number counts can be approximated by a power-law:

$$\frac{dN}{dm} \propto 10^{\kappa m}. \quad (27)$$

To infer the true number count-magnitude relation, we need to ensure that our catalog is free from contaminants since not all extended sources from the XSC are external galaxies. At low Galactic latitude where stellar density is high, unresolved multiple star systems are often confused as extended sources. For the purpose of fitting for the power-law slope  $\kappa$ , we use only sources with  $|b| > 30^\circ$ . Using  $\sim 250,000$  galaxies in the magnitude range  $13.2 < m < 13.7$  (where the reliability has been determined to be 99% by Huchra & Mader [24]), we fitted a number count slope  $\kappa = 0.676 \pm 0.005$ .

While the XSC is unreliable at low Galactic latitudes, the  $|b| > 30^\circ$  cut is too permissive and would throw away a large area of the sky that can be used for analysis. In principle, we could use the stellar density  $n_{star}$  from the 2MASS Point-Source Catalog(PSC) to set a threshold for excluding region of high stellar density. However, since it has been shown by [3] and [25] that unresolved extended galaxies are found in the PSC(up to 2% of all point sources with  $K_{20} \sim 14$ ), a mask derived from the observed stellar density would preferentially exclude regions of high galaxy density.

We use the extinction map of [43] to exclude regions of the sky where the XSC is unreliable. Figure 2 shows the average number of galaxies per HEALPix pixel of  $0.83 \text{ deg}^2$  ( $N_{side} = 64$ ), as a function of Galactic extinction for the four magnitude ranges used in our analysis. For bright galaxies, e.g.  $K_{20} < 13.5$ , the Galactic density is constant on degree scales. For the faintest magnitude bin, the number density drops off at large  $A_K$  for

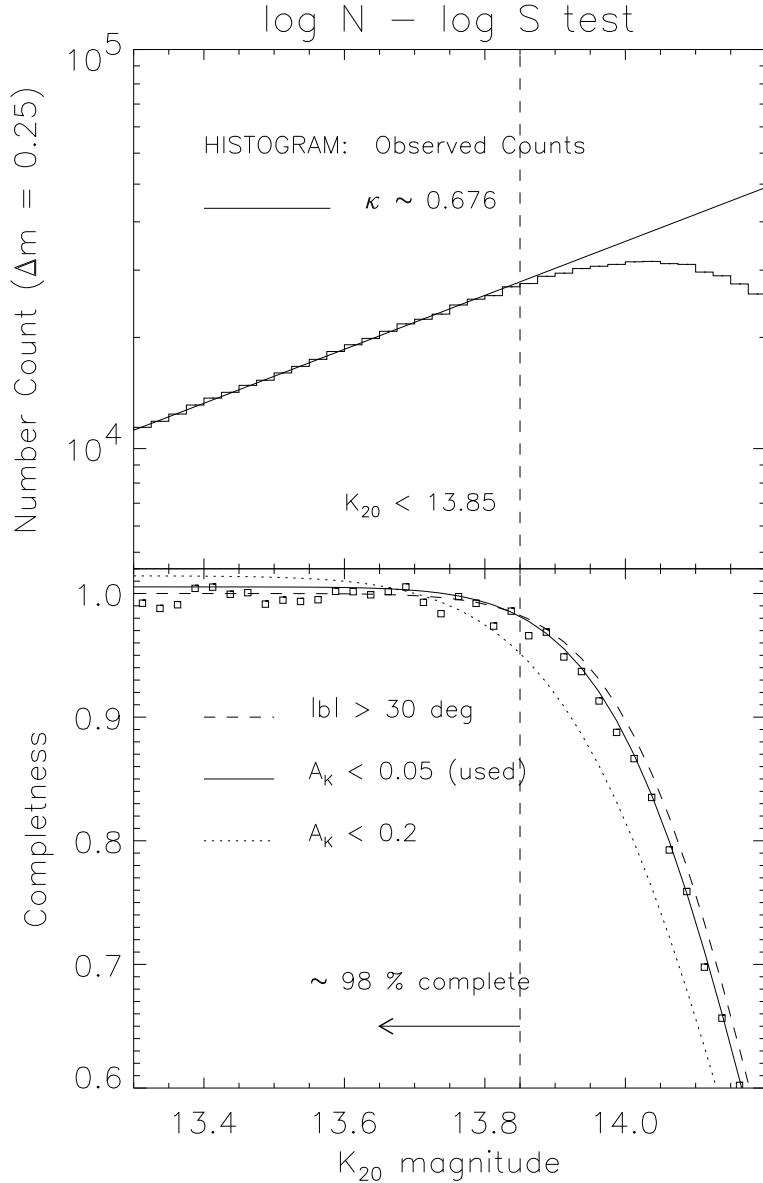


FIG. 1: (Top panel) The histogram is the observed  $K_{20}$  number-magnitude relation for galaxies in regions with  $A_K < 0.05$ . The solid line is the model counts inferred using data from  $|b| > 30^\circ$  in the magnitude range  $13.2 < K_{20} < 13.7$  where the extended source catalog(XSC) is most reliable. (Bottom panel) The square points gives the completeness as inferred from the difference between the observed and model counts. The *solid* curve is a fit to a parametric model that estimates both the incompleteness and contamination rate in a consistent manner. The *dotted* curve is a similar fit using data with a less stringent  $A_K < 0.2$ . The *dashed* curve is from  $|b| > 30^\circ$ , which serves roughly as the completeness upper-bound for the XSC. The vertical line at  $K_{20} = 13.85$  gives a completeness at 98% for data with  $A_K < 0.05$  used in our analysis.

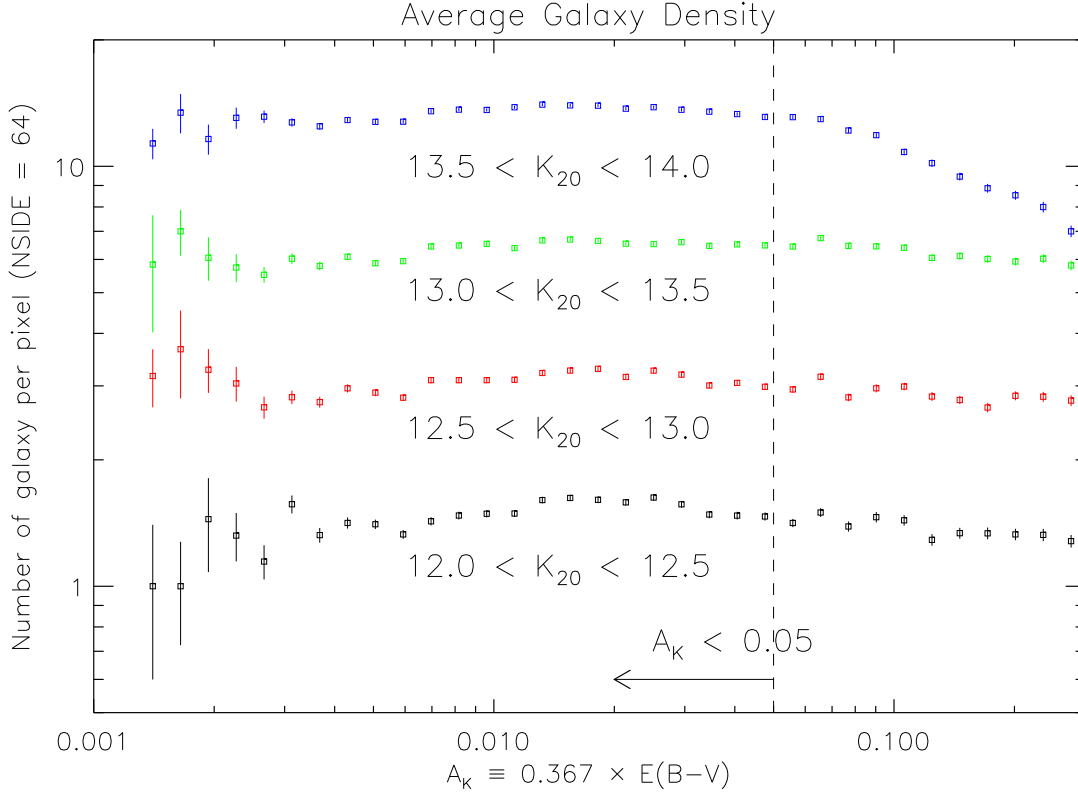


FIG. 2: Average number of galaxies per  $0.83 \text{ deg}^2$  pixel (HEALpix  $N_{side} = 64$ ) as a function of extinction. For bright galaxies ( $K_{20} < 13.5$ ), the galaxy density is constant up to extinction value  $\sim 0.25$ . For  $13.5 < K_{20} < 14.0$ , the density drops off at  $A_K \sim 0.65$ . We use only regions with  $A_K < 0.05$  (dashed vertical line) for our analysis. Errors are estimated using jack-knife resampling.

$A_K$  beyond  $\sim 0.065$ . We thus choose  $A_K < 0.05$  [55]. This stringent threshold excludes  $\sim 99\%$  of all regions with  $n_{star} > 5000 \text{ deg}^{-2}$ . Moreover, it improves the global reliability of galaxy counts, as our flux indicator  $K_{20}$  for each source was corrected for Galactic extinction, which has an uncertainty that scales with  $A_K$  itself. This cut reduces the number of extended sources with  $K_{20} < 14.3$  to  $\sim 1$  million, covering  $\sim 68.7\%$  of the sky. For the sake of completeness, we also repeat our cross-correlation analysis for a less stringent mask with  $A_K < 0.1$ , which covers  $\sim 79.0\%$  of the sky.

Using  $\kappa = 0.676$  derived from regions with  $|b| > 30^\circ$  as a model for the true underlying number counts, we infer the catalog completeness and contamination as a function of apparent magnitude for the extinction cropped sky. We deduce the intercept of the linear log counts - magnitude model by scaling the observed number counts from the  $|b| > 30$  region

to the larger  $A_K$  masked sky at the bright magnitude range  $12.5 < K_{20} < 13.0$ . Essentially, we assumed the two number count distributions are identical at those magnitudes. The observed fractional deviation from Eq. (27)

$$I(m) = \left( \frac{dN^\kappa}{dm} - \frac{dN^{\text{obs}}}{dm} \right) / \frac{dN^\kappa}{dm} \quad (28)$$

is positive at faint magnitudes indicating incompleteness but crosses zero to a constant negative level towards the bright-end, which we inferred as contamination to the XSC. Plotted in the bottom panel of Figure 1 is the completeness function  $C(m) \equiv 1 - I(m)$ , where we parametrically fitted using

$$I(m) = I_o \exp \left[ -\frac{(m - \bar{m})^2}{2\sigma^2} \right] - \text{Const.} \quad (29)$$

In Figure 1, the term *Const* describes the low level of excursion beyond  $C(m) = 1$ . We obtained a  $\sim 98\%$  completeness for  $K_{20} < 13.85$  and contamination rate at  $0.5\%$  level for  $A_K < 0.05$  (solid curve). As a comparison, a less stringent threshold of  $A_K < 0.2$  (dotted curve), the completeness is  $\sim 95\%$  with contamination at  $1.5\%$ . The dashed curve is computed using high latitude data ( $|b| > 30^\circ$ ), serves roughly as the completeness upper-bound (as a function of apparent magnitude) for the XSC.

At a low level, contaminants in the catalog merely increase the noise of our signal with marginal systematic bias. The  $A_K < 0.05$  extinction mask is close to optimal in terms of signal-to-noise for our cross-correlation analysis. On the other hand, catalog incompleteness at faint magnitudes affects our ability to infer the correct redshift distribution. We use galaxies up to  $K_{20} = 14.0$  but weighted the redshift distribution at a given magnitude range (described below) by Eq. (29).

## 2. Redshift Distribution

The redshift distribution of our sample was inferred from the Schechter [42] parameters fit of the  $K_{20}$  luminosity function from [28]. The redshift distribution,  $dN/dz$  of galaxies in the magnitude range  $m_{\text{bright}} < m < m_{\text{faint}}$  is given by the integration of the luminosity function  $\Phi(M)$

$$\frac{dN}{dz}(z) dz = \int_{M_b(z)}^{M_f(z)} \Phi(M) dM \times \frac{dV_c}{dz}(z) dz, \quad (30)$$

TABLE I:  $\frac{dN}{dz}$  parameters for the four magnitude bins

	$z_o$	$\beta$	$\lambda$	$N$
$12.0 < K_{20} < 12.5$	0.043	1.825	1.574	49817
$12.5 < K_{20} < 13.0$	0.054	1.800	1.600	102188
$13.0 < K_{20} < 13.5$	0.067	1.765	1.636	211574
$13.5 < K_{20} < 14.0$	0.084	1.723	1.684	435232

where  $dV_c/dz$  is the line-of-sight comoving volume element and

$$M_f(z) \equiv m_{\text{faint}} - DM(z) - k(z) \quad (31)$$

$$M_b(z) \equiv m_{\text{bright}} - DM(z) - k(z) \quad (32)$$

Here,  $DM(z)$  and  $k(z)$  are the distance modulus and  $k$ -correction at redshift  $z$ . To be consistent with [28], we employ  $k(z) = -6.0 \log(1 + z)$ , but the redshift distribution is insensitive to the exact form of the  $k$ -correction. The Schechter parameters used were  $M^* = -23.39$  and  $\alpha_s = -1.09$ . For analytic convenience, we further model  $dN/dz$  with the three parameter generalized-gamma distribution:

$$\begin{aligned} \frac{dN}{dz}(z | \lambda, \beta, z_o) dz &\propto \frac{\beta}{\Gamma(\lambda)} \left(\frac{z}{z_o}\right)^{\beta\lambda-1} \\ &\times \exp\left[-\left(\frac{z}{z_o}\right)^\beta\right] d\left(\frac{z}{z_o}\right). \end{aligned} \quad (33)$$

The fit were weighted by relative counts, hence they are exact near  $z_o$ , the mode of the distribution, but underestimate the true number at the high redshift tail by less than 1%. Table I gives the redshift distribution parameters for the four magnitude bins used in our analysis. We normalize the integral of  $dN/dz$  with the total number of observed galaxies in the respective magnitude range,

$$N_{\text{total}}(\Delta\Omega) = \int_0^\infty \frac{dN}{dz}(z) dz \times \Delta\Omega \quad (34)$$

$$\begin{aligned} &= \int_0^\infty n_c(z) \frac{dV_c}{dz}(z) dz \int d\Omega \\ &\equiv \int n_c(r) r^2 dr d\Omega. \end{aligned} \quad (35)$$

The observed  $N_{\text{total}}$  is consistent with the 10% uncertainty in the normalization,  $\phi^* = 1.16 \times 10^{-2} h^3 \text{ Mpc}^{-3}$  obtained by [28] in their luminosity function analysis. Eq. (35) gives

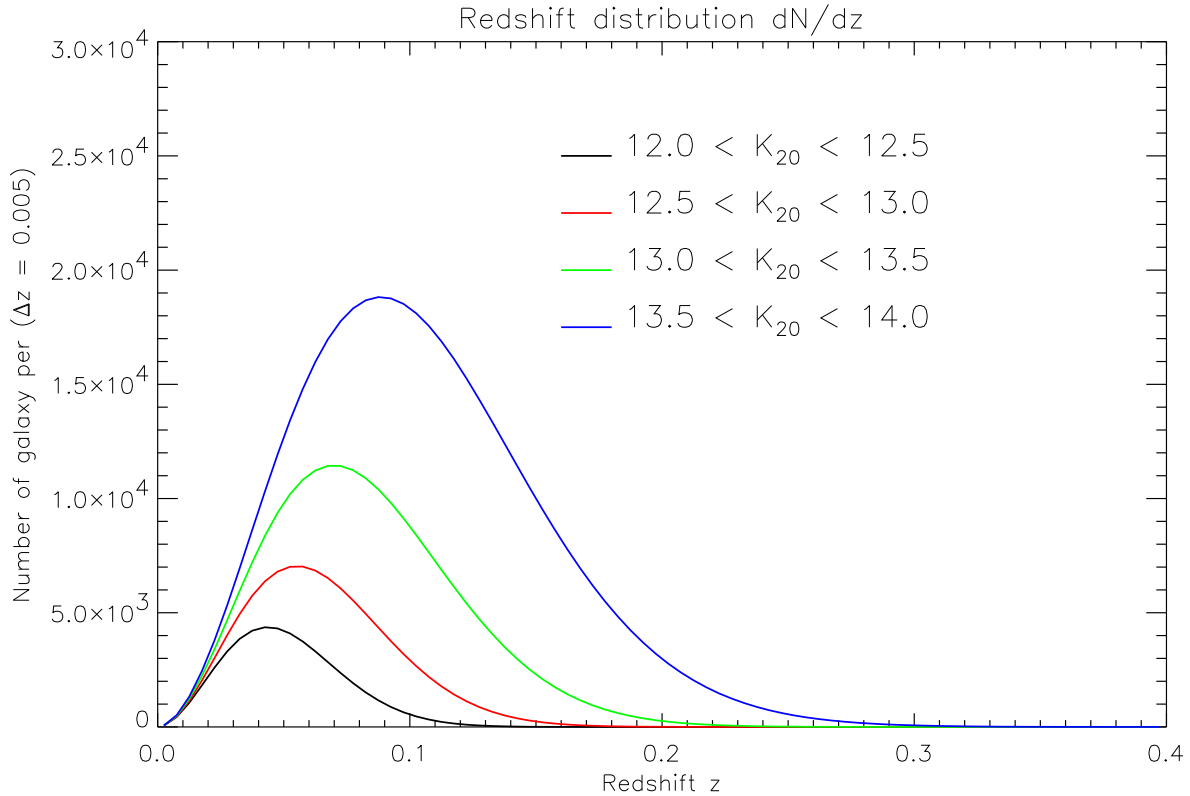


FIG. 3:  $dN/dz$  for the four magnitude bins used in the analysis.

the explicit relation (in the absence of clustering) between the redshift distribution,  $dN/dz$ , and the comoving density,  $n_c(r)$  used in Sec. III.A.

Figure 3 is a plot of the redshift distribution for the four magnitude bins used in our analysis. For the first three bright samples, where we are complete, the parameters for  $dN/dz$  were derived from a direct application of Eq. 30. For  $13.5 < K_{20} < 14.0$ , the redshift distribution was computed by summing up magnitude slices with interval  $\Delta K_{20} = 0.05$ , and weighted by their relative number counts.

## V. RESULTS

For the following results, unless we mention otherwise, we use the WMAP concordance cosmological model.

By comparing the angular auto-power spectrum of the galaxies in each magnitude bin with the theoretical auto-power spectrum (Eq.19), we can obtain the bias of the 2MASS galaxies. In order to do this, we use a  $\chi^2$  fit, assuming independent gaussian random errors

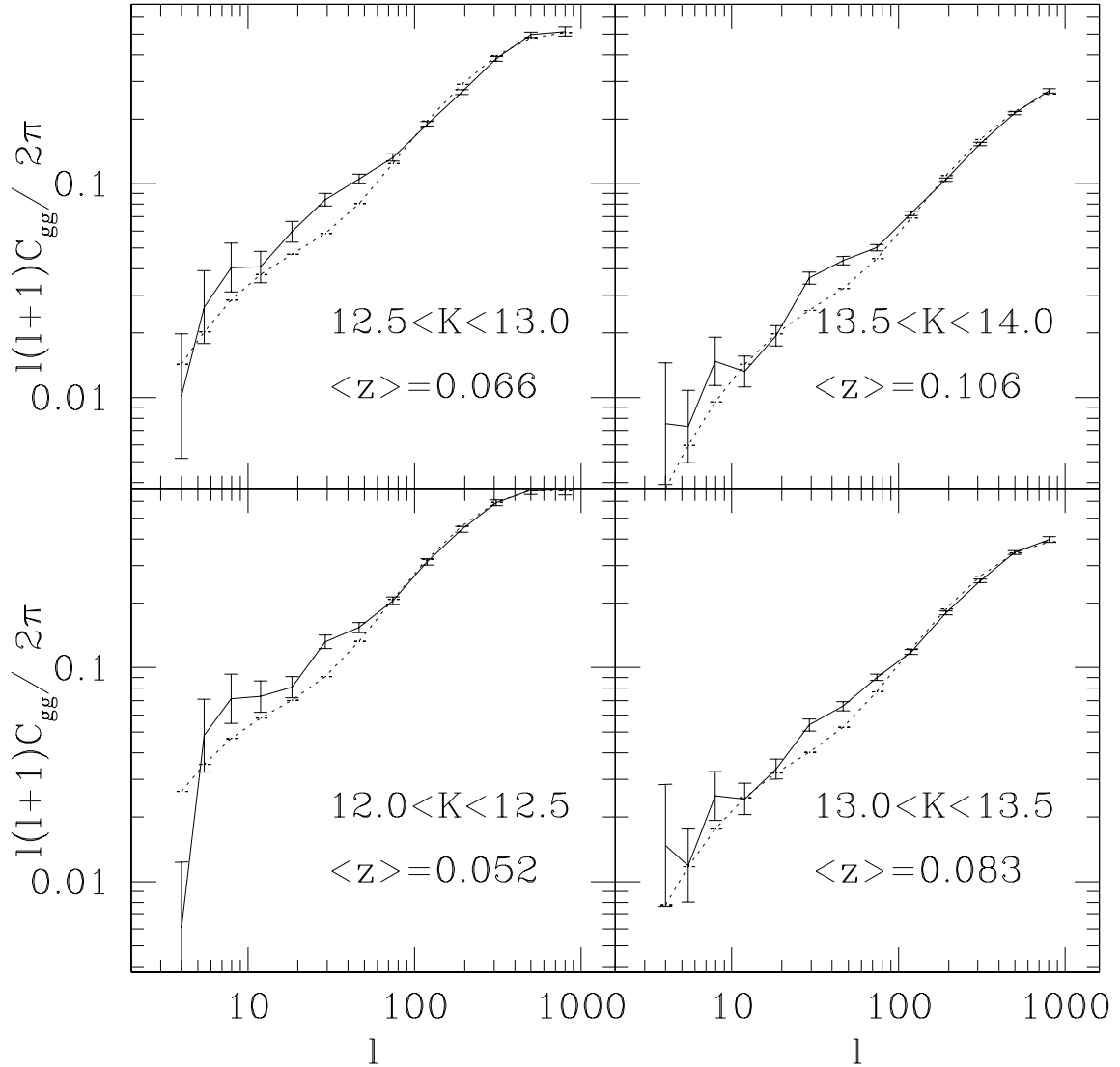


FIG. 4: The auto-power for our four different magnitude bins. The solid curves show the observed auto-power multipoles with their estimated Gaussian errors (Eq.23), while the dashed curves are the projected Peacock and Dodds [37] non-linear power spectra with the best fit constant bias. The best fit Poisson noise term is subtracted out.

at each  $\ell$ -bin. Figure 4 compares our best fit models of the auto-power (solid curves) with the measured auto-powers for each magnitude bin. The value of the bias for all the magnitude bins is within

$$b_g = 1.11 \pm 0.02, \quad (36)$$

which confirms our constant bias assumption[56]. Our values for the Poisson correction factor (see Eq.19),  $\gamma$ , are all within 1% of 1.02. The most significant deviation of the theoretical fit from the observed auto-power is about 30% at  $\ell \sim 30 - 40$ . Since this portion of  $\ell$ -space does not make any significant contribution to either the ISW signal(which is significant for  $\ell < 20$ , see Figure 7), or the SZ or point source signals(which may be significant for  $\ell > 100$ , see Figure 7), a possible systematic error at this scale does not affect our measured signals significantly. In fact, if this discrepancy is due to foreground contamination or observational systematics of the 2MASS survey (which do not correlate with the signal), then by using the observed auto-power to construct our covariance matrix (see Sec. III.C), we already have included it in our errors.

The angular scale corresponding to  $\ell = 30 - 40$  is a few degrees, which is close to the length of the 2MASS scanning stripes ( $6^\circ$ ). The amplitude of deviation implies systematic fluctuations of order 10% in the number counts on that scale. If these were due to systematic errors in the 2MASS photometric zero-point, such fluctuations require a magnitude error  $\Delta m \sim 0.06$ , which is significantly larger than the calibration uncertainties in 2MASS [35].

The points in Figure 5 summarize our twelve observed cross-correlation functions (3 WMAP bands  $\times$  4 magnitude bins), while Figure 6 shows the same data after subtracting out the best fit contribution due to microwave Point Sources. We fit our theoretical model (Eq. 18) to our cross-correlation points (including only the W-band for the first 4  $\ell$ -bin; see Sec. III.C), allowing for free global normalizations for the ISW, SZ and Point Source components. The curves show this model with the best fit normalizations for these components, while the shaded region shows the 68% uncertainty around a null hypothesis. Figure 7 shows how individual theoretical components depend on frequency and  $\ell$  for our faintest magnitude bin. As we mentioned in Sec. III.C, different  $\ell$ -bins are nearly independent. However, different combinations of frequency bands and magnitude bins are highly correlated and we use the full covariance matrix which we obtain from the data itself (see III.C) for our  $\chi^2$  analysis.

The apparent dispersion in our data points for the first 4-5  $\ell$ -bins is smaller than what we expect from gaussian statistics (the shaded regions in Figures 5 and 6). This may be due to the non-gaussian nature of the systematics (observational or Galactic), which dominate the error on large angles, and make the variance (Eq. 23) significantly different from the 68% confidence region.

Figures 5 & 6 show that our faintest magnitude bin has the smallest error. This is due

to the fact that our faintest magnitude bin covers the largest effective comoving volume and number of galaxies (see Table I and Figure 3), and as a result, between 50-70% of our signal (depending on the component) comes from this bin. Repeating the statistical analysis for individual magnitude bins leads to results consistent with the combined analysis within the errors.

### A. Thermal SZ signal

In a model described in Appendix A, we quantify the amplitude of the SZ signal in terms of  $Q$ , the coefficient of temperature-mass relation for clusters of galaxies

$$T_e(M) = (6.62 \text{ keV})Q \left( \frac{M}{10^{15}h^{-1}M_\odot} \right)^{2/3}. \quad (A2)$$

Different theoretical and observational methods place  $Q$  somewhere between 1 and 2, with observations preferring the higher end. This amplitude could be equivalently described in terms of  $\tilde{T}_e$ , the product of pressure bias and average electron temperature (see Eq.7), which is less model dependent. Our best fit value for the thermal SZ signal, which shows a signal at the  $3.1\sigma$  level, is

$$Q = 0.62 \pm 0.2, \text{ or } \tilde{T}_e = b_p \bar{T}_e = (0.54 \pm 0.17) \text{ keV}. \quad (37)$$

This result is slightly dependent on the spectrum of the microwave point sources, which we discuss below in V.C. If we restrict the analysis to  $\ell > 20$ , which is where all the SZ signal comes from and our estimates of the covariance matrix is robust, our reduced  $\chi^2$  is 0.93 which is within the 68% allowed range for our  $12 \times 13$  degrees of freedom. This implies that there is no observable systematic deviation from our theoretical expectation for the shape of the thermal SZ cross-power (or its gaussianity).

Our low level of detection for the thermal SZ effect is consistent with the non-detection of a WMAP cross-correlation with the ROSAT X-ray map in [14].

If we take this  $2\sigma$  deviation from the canonical value at face value, there could, at least, be four possible explanations:

- 1- The environments of galaxy groups with masses of a few  $\times 10^{13}M_\odot$  are in fact colder than what we expect from adiabatic evolution and shock heating. This may be due to an efficient cooling mechanism.

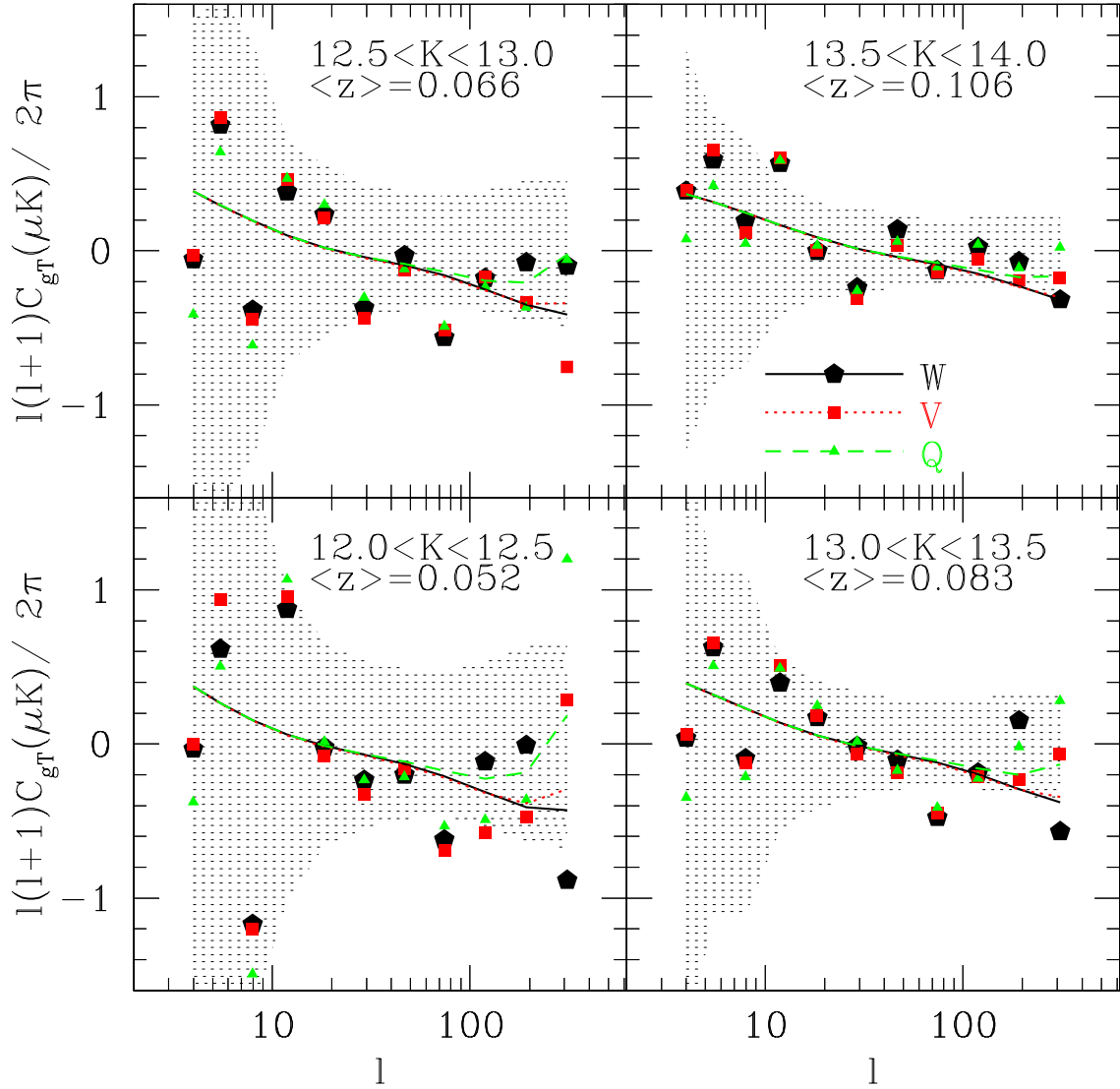


FIG. 5: The cross-power for our four magnitude bins. The curves are the best fit model (ISW+SZ+Point Sources) for the three bands and the points show the data. The ISW/SZ components dominate the signal for  $\ell$ 's below/above 20. The Point Source contribution becomes important for the lower frequency bands at the highest  $\ell$ 's. The shaded region shows the  $1 - \sigma$  error centered at the null hypothesis. Note that, while different  $\ell$ -bins are nearly independent, different cross-powers of bands with magnitude bins are highly correlated. As shot noise dominates the signal for our last two  $\ell$ -bins, for clarity, we only show the first 11  $\ell$ -bins, for which the errors for the three WMAP bands are almost the same.

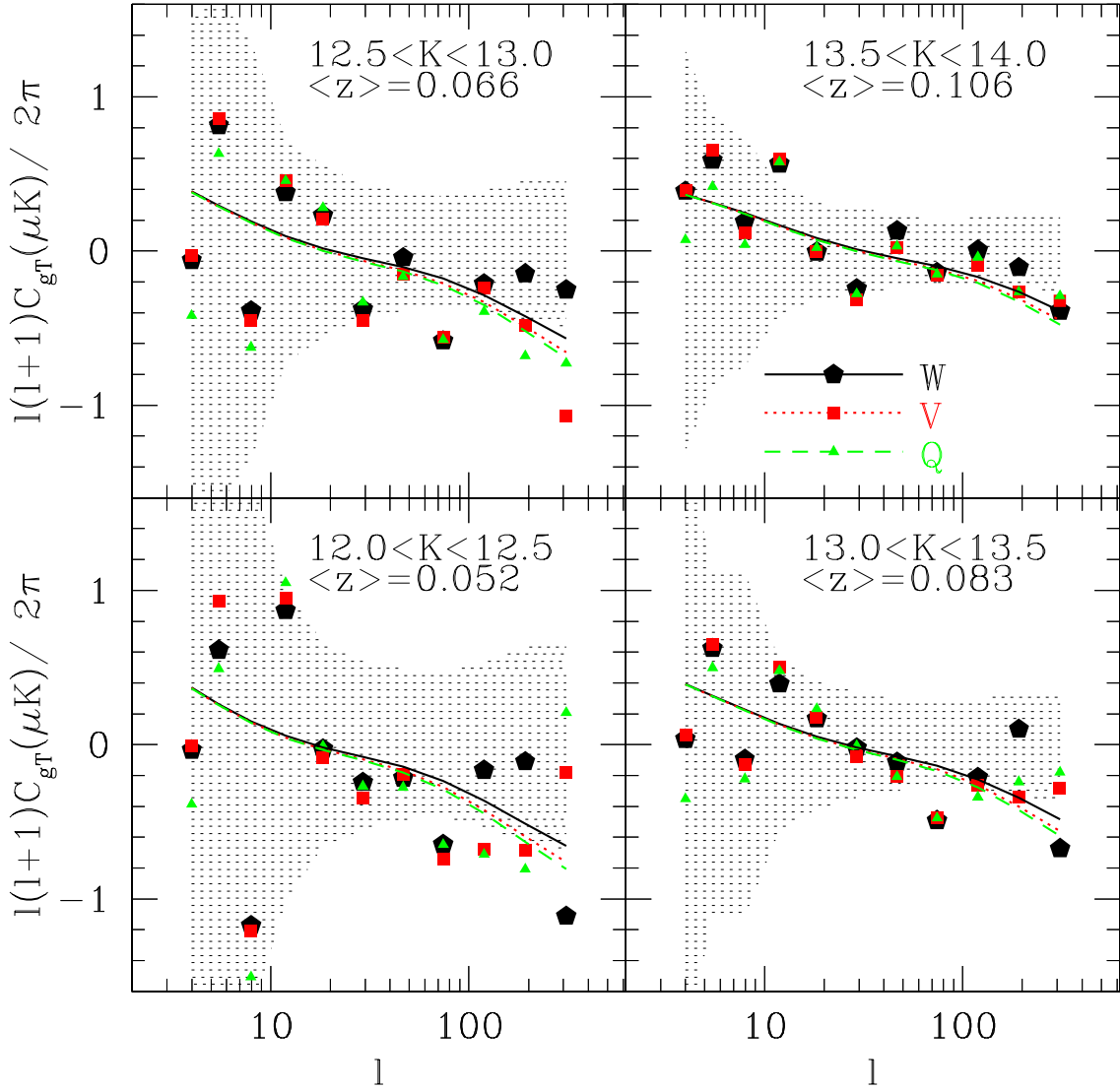


FIG. 6: The same as Figure 5, but with the Point Source contributions subtracted from both theory and data.

2- The observations of the cluster mass-temperature relation probe the gas temperature weighted by X-ray free-free emission ( $\propto n_e^2 T_e^{1/2}$ ), while the thermal SZ average temperatures are weighted by the electron density,  $n_e$ . If the gas is hotter where the electron density is higher (e.g. close to the center of the cluster), the X-ray observations systematically overestimate the SZ temperature and  $Q$ [30]. On the other hand, all the theoretical estimates are based on the equipartition of energy among electrons and ions. The thermalization process may not be efficient in the outer regions of a cluster, leading to a lower temperature

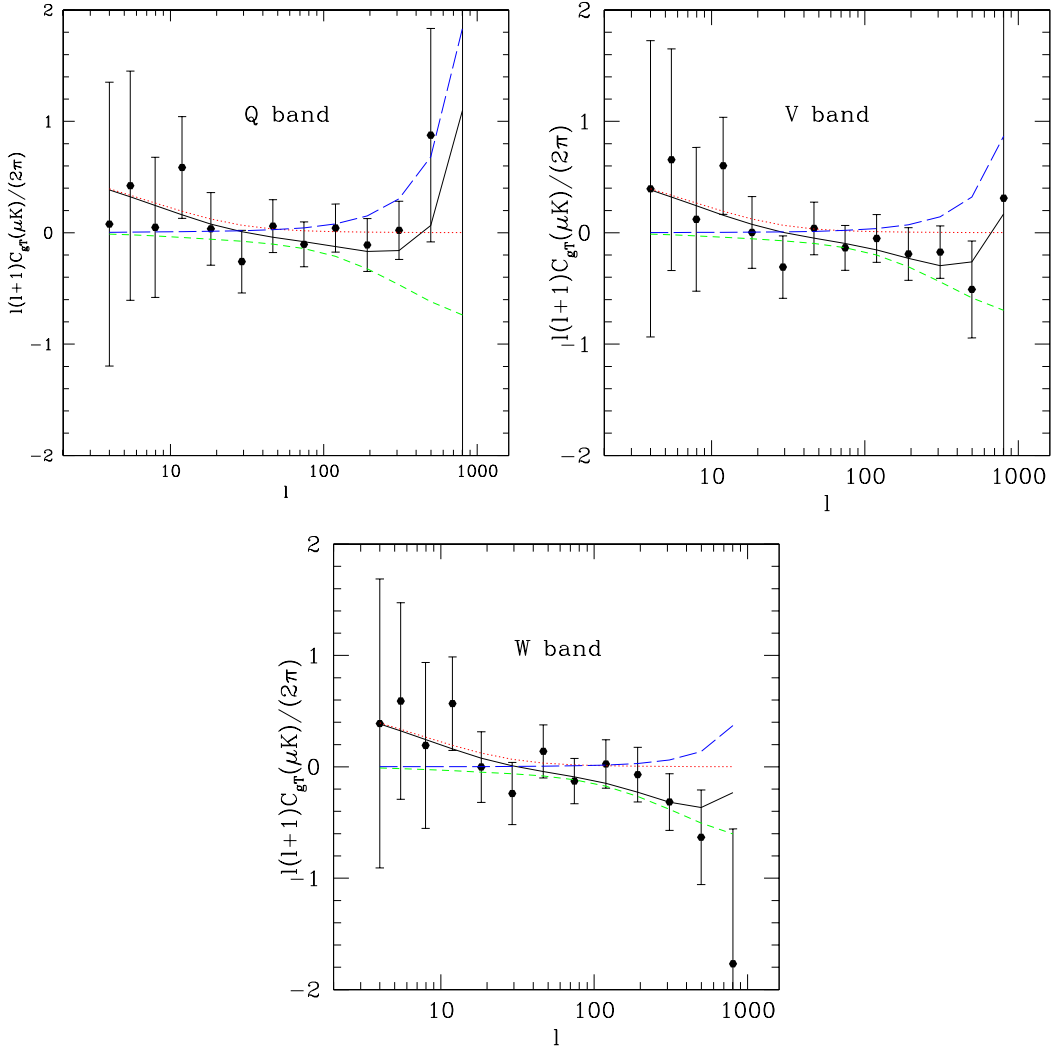


FIG. 7: Different components of our best fit theoretical cross-power model, compared with the data for our faintest magnitude bin ( $13.5 < K < 14$ ). The dotted(red) curves show the ISW component, while the short-dashed(green) and long-dashed(blue) curves are the SZ and Point Source components respectively. The black curves show the sum of the theoretical components, while the points are the observed cross-power data.

for the electrons[18], and thus a lower  $Q$ . Also, analytical estimates which are based on virialization(e.g. [2, 30]) may fail in these regions, which has a similar effect.

3- Since the thermal SZ effect is most sensitive to the value of  $\sigma_8$ , rather than other cosmological parameters, it may be that  $\sigma_8$  is actually lower than the WMAP concordance model. Investigating Eq.(A5) for  $0.6 < \sigma_8 < 0.9$ , one can see that what we measure by our cross-correlation analysis is approximately proportional to  $Q\sigma_8^{4.3}$ . Assuming  $1 < Q < 2$

leads to  $0.58 < \sigma_8 < 0.80$  at the  $1\sigma$  level.

4- Although we do not see its signature in the reduced  $\chi^2$ , there still may be systematic deviations from our simple theory of thermal SZ, developed in II.B and Appendix A. For example, galactic superwinds might be able to reduce correlation among galaxies and hot gas, as they cause the hot gas to fragment.

Repeating the analysis with the  $A_K < 0.1$  extinction mask (See Sec. IV.B.1) for the 2MASS galaxies, which has a 10% larger sky coverage, increases the SZ signal slightly to  $Q = 0.66 \pm 0.18$ , which is a detection at the  $\sim 3.7\sigma$  significance level. This is probably because the Galactic contamination close to the plane is only at large angles and does not contribute to the SZ signal. Therefore, as long as the Galactic contamination does not completely dominate the fluctuations, increasing the area only increases the SZ signal.

## B. ISW signal

Our  $\chi^2$  fit yields an ISW signal of

$$\text{ISW} = 1.53 \pm 0.62 \quad (38)$$

$\times$  concordance model prediction,

a  $2.5\sigma$  detection of a cross-correlation. As with the previous cross-correlation analyses[8, 16, 17, 36], this is consistent with the predictions of the concordance  $\Lambda$ CDM paradigm. However, among the three signals that we try to constrain, the ISW signal is the most difficult to extract, because almost all the signal comes from  $\ell < 20$ , given our redshift distribution. For such low multipoles, there are several potential difficulties:

1- The small Galactic contamination or observational systematics in 2MASS may dominate the fluctuations in the projected galaxy density at low multipoles and wipe out the signal. However, since we use the observed auto-power of 2MASS galaxies for our error estimates, this effect, which does contribute to the auto-power (and not to the signal), is included in our error.

2- Our covariance estimator loses its accuracy as the cosmic variance becomes important at low multipoles (see III.C). A random error in the covariance matrix can systematically increase the  $\chi^2$  and hence decrease the estimated error of our signal. However, our reduced

TABLE II: Best fit point source strengths for different assumed spectra. The associated best fit SZ signal and  $\chi^2$  are also quoted. Here,  $T_A$  stands for the antenna temperature, while  $L_V^*$ , defined in Eq.(B2), is the estimated luminosity of the Milky Way in WMAP's V-band.

Spectrum	$L_V/L_V^*$	$Q$	$\chi^2$
Milky Way	$16.2 \pm 7.8$	$0.57 \pm 0.21$	111.2
$\delta T_A \propto \nu^{-2}$	$21.0 \pm 8.1$	$0.62 \pm 0.20$	109.5
$\delta T_A \propto \nu^{-3}$	$10.9 \pm 4.7$	$0.49 \pm 0.17$	110.8

$\chi^2$  is 0.88, which is in fact on the low side (although within  $1\sigma$ ) of the expected values for 124 degrees of freedom (remember that we only used the W band for the first 4  $\ell$ -bins). Assuming gaussian statistics, this implies that we do not significantly underestimate our error.

3- Possible Galactic contamination in WMAP may correlate with Galactic contamination in 2MASS at low multipoles, which may lead to a fake positive signal. However, the largest contribution of Galactic foreground is visible in the Q-band [6], and our low  $\ell$  multipoles have in fact a lower amplitude in Q band. Although this probably shows a large error due to contamination in the Q-band amplitude, the fact that this is lower than the amplitude of V and W bands implies that our main signal is not contaminated. Because of the reasons mentioned in III.C, we only use the W-band information for  $\ell < 14$ .

Using the less stringent extinction mask,  $A_K < 0.1$  (see IV.B.1), for the 2MASS sources yields a signal of  $ISW = 1.9 \pm 1.1$ , which is a lower signal to noise detection at the  $1.7\sigma$  level. This is probably due to the fact that most of the ISW signal comes from angles larger than  $\sim 10^\circ$ , which is highly contaminated in regions close to the Galactic Plane.

Finally, we should mention that since the ISW signal comes from small  $\ell$ 's, while the SZ and point source signals come from large  $\ell$ 's (See Figure 7), there is a small correlation (less than 10%) between the ISW and other signals.

### C. Microwave Point Sources

As described in II.C, we assume that our point sources trace the 2MASS objects and have either a Milky Way spectrum, a  $\nu^{-2}$ , or a  $\nu^{-3}$  frequency dependence their antenna

temperature (the last two are the expected synchrotron spectrum of radio sources). The results are shown in Table II. We see that, although all the spectra are consistent at a  $2\sigma$  level, we achieve the lowest  $\chi^2$  for a  $\nu^{-2}$  spectrum which is similar to the spectrum of point sources, identified by the WMAP team [6]. We should also note that since the  $\ell$ -dependence of the SZ and Point Source signals are very similar, the two signals are correlated at a 50 – 70% level, which is shown in Figure 8. Using a less stringent extinction mask ( $A_K < 0.1$ , see IV.B.1) increases the detection level of microwave sources by about 10%.

To relax our assumption for the redshift distribution of Point Sources (which we assume to be the same as 2MASS sources at each magnitude bin; see II.C), we can also allow different magnitude bins to have different  $L_V$ 's and treat each as a free parameter. It turns out that this does not affect either our ISW or SZ signals, or their significance, while  $L_V$ 's for each magnitude bin is consistent with the values in Table II, within the errors. As the Point Source signal is dominated by Poisson noise at large  $\ell$ 's, removing the assumed clustering among the Point Sources (see II.C), does not affect the SZ or ISW signals either.

## VI. CONCLUSIONS

We obtain the cross-power spectrum of the three highest frequency bands of the WMAP cosmic microwave background survey with the 2MASS Extended Source Catalog of near infrared galaxies. We detect an ISW signal at the  $\sim 2.5\sigma$  level, which confirms the presence of a dark energy, at a level consistent with the WMAP concordance cosmology. We also find evidence for an anti-correlation at small angles (large  $\ell$ 's), which we attribute to thermal SZ. However, the amplitude of this signal is at least 40% ( $\simeq 2\sigma$ ) less than the predictions of simplest SZ models. Finally, we see a signal for microwave Point Sources at the  $2.6\sigma$  level.

We've seen that the completeness limit of the extended source catalog is between 13.5 and 14 in K. However, matches with SDSS show that there are many unresolved sources in the 2MASS Point Source Catalog (PSC) that are in fact galaxies. If we can select out galaxies in the PSC, perhaps by their distinctive colors, we should be able to push the sample at least half a magnitude fainter than we have done here, probing higher redshifts with a substantially larger sample.

Future wide-angle surveys of galaxies should be particularly valuable for cross-correlation with the WMAP data, especially as the latter gains signal-to-noise ratio in further data

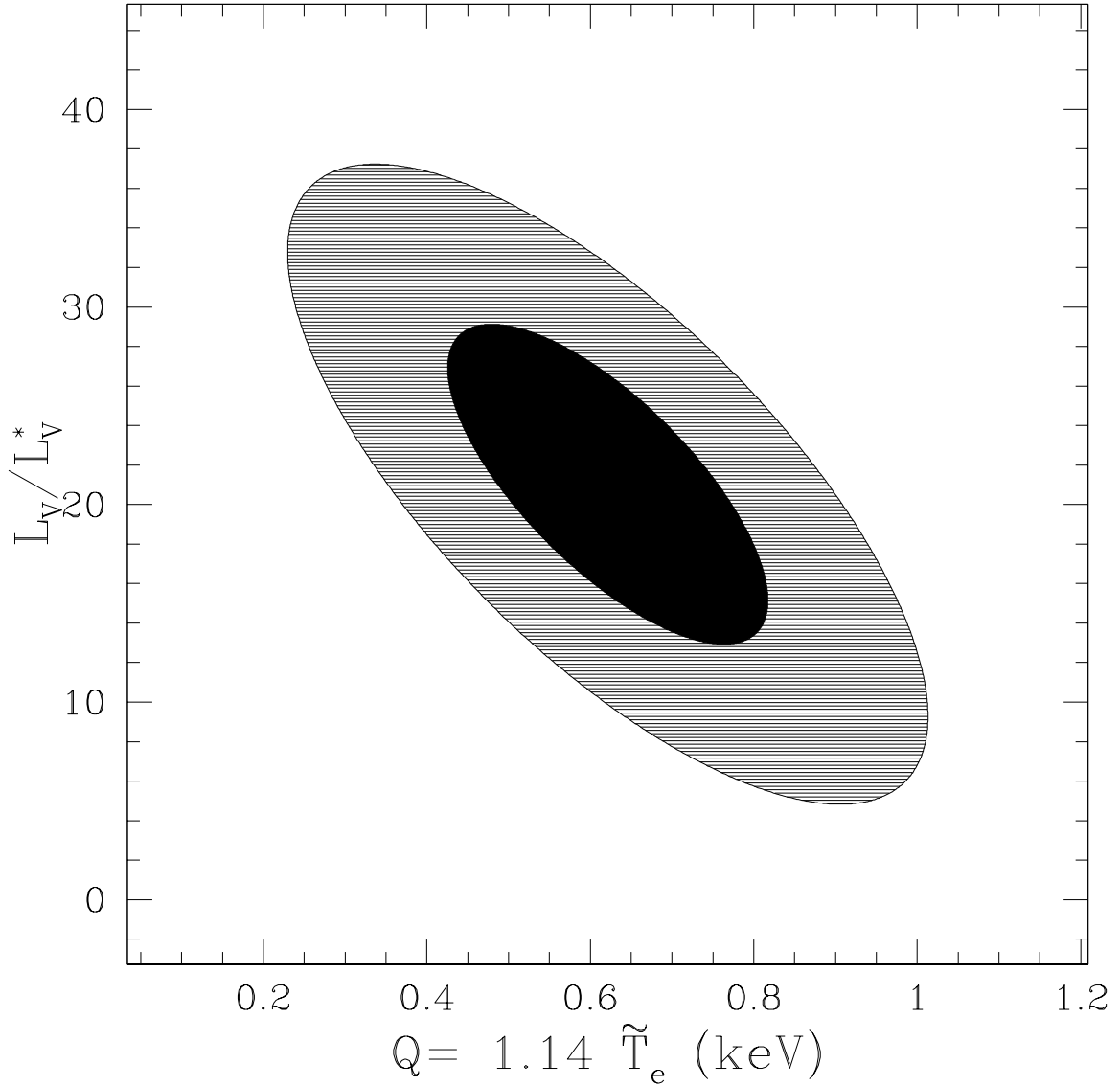


FIG. 8: 1 and  $2 - \sigma$  likelihood regions of our SZ+Point Source signals, for a  $\delta T_A \propto \nu^{-2}$  spectrum (see Table II).  $Q$  (defined in Eq.A2) is the coefficient of the mass-temperature relation for galaxy clusters, while  $\tilde{T}_e$  (defined in Eq.7), is the product of gas pressure bias and the average electron temperature.  $L_V$  is the average WMAP V-band luminosity of the 2MASS sources, while  $L_V^*$  (defined in Eq.B6) is the same number, estimated for the Milky Way. The large correlation of  $Q$  (SZ signal) and  $L_V$  (Point Source signal) is due to the similar  $\ell$ -dependence of the two signals (see Figure 7). Note that the conversion between  $\tilde{T}_e$  and  $Q$  depends on the assumed cosmological model (see Appendix A).

releases. The Pan-STARRS project [27] for example, should yield a multi-color galaxy catalog to 25th mag or even fainter over 20,000 square degrees or more of the sky well before the end of the decade; it will more directly probe the redshift range in which the SZ and ISW kernels peak, and therefore should be particularly valuable for cross-correlating with WMAP and other CMB experiments.

### Acknowledgments

NA wishes to thank David N. Spergel for the supervision of this project. We would like to thank Eiichiro Komatsu and Christopher Hirata for illuminating discussions and helpful suggestions, Doug Finkbeiner for help on the analysis of WMAP temperature maps, and R.M. Cutri and Mike Skrutskie on the 2MASS dataset. MAS acknowledges the support of NSF grants ASF-0071091 and AST-0307409.

---

- [1] Abell, G.O., Corwin, H., Olwin, R., 1989, ApJS, 70, 1
- [2] Afshordi, N., & Cen, R. 2002, ApJ, 564, 669
- [3] Bell, E.F., et al. 2003, astroph/0302543
- [4] C. Bennett et al. , ApJ, 464, L1 (1996)
- [5] Bennett, C.L. *et al.* 2003, astro-ph/0302207, the public data and other WMAP papers are available at <http://lambda.gsfc.nasa.gov/product/map>
- [6] Bennett, C.L. *et al.* 2003, astro-ph/0302208
- [7] Boughn, S. P., Private Communication.
- [8] Boughn, S. P. & Crittenden, R. G., Phys. Rev. Lett. 88, 021302 (2002)
- [9] Boughn, S. P. & Crittenden, R. G. 2003, astro-ph/0305001
- [10] Condon, J. et al. 1998, Astron. J. 115, 1693
- [11] Cooray, A. 2002, Phys. Rev. D, 65, 083518
- [12] Corasaniti, P.S. *et al.* 2003, Phys.Rev.Lett. 90, 091303
- [13] Crittenden, R.G., & Turok, N. 1996, PRL, 76, 575
- [14] Diego. J.M., Silk J., & Sliwa 2003, astro-ph/0302268
- [15] Efstathiou, G. 2003, astro-ph/0307515

- [16] Fosalba P., & Gaztañaga E. 2003, astro-ph/0305468
- [17] Fosalba P., Gaztañaga E., & Castander, F.J. 2003, astro-ph/0307249
- [18] Fox, D.C., & Loeb, A. 1997, ApJ, 491, 459
- [19] Gorski, K. M., Hivon, E., & Wandelt, B. D. 1998, in *Evolution of Large-Scale Structure: From Recombination to Garching*
- [20] Gunn, J., Gott, J. 1972, ApJ, 176, 1
- [21] Hivon, E., Gorski, K. M., Netterfield, C. B., Crill, B. P., Prunet, S., & Hansen, F. 2002, ApJ, 567, 2
- [22] Hinshaw, G., et al. 2003, astro-ph/0302217
- [23] Hu, W. & Dodelson, S. 2002, ARA&A, 40, 171
- [24] Huchra, J & Mader, J (2000) at <http://cfa-www.harvard.edu/~huchra/2mass/verify.htm>
- [25] Ivezić, Ž. et al. in *IAU Colloquium 184: AGN Surveys, 18-22 June 2001, Byurakan (Armenia)*
- [26] Jarrett, T.H., et al. 2000, AJ, 119, 2498
- [27] Kaiser et al. 2002, SPIE, 4836, 154
- [28] Kochanek, C.S., et al. 2001, ApJ 560, 566
- [29] Kogut, C.L. et al. 2003a, astro-ph/0302213
- [30] Komatsu, E., & Seljak, U 2001, MNRAS, 327, 1353
- [31] Limber, D.N. 1954, ApJ, 119, 655
- [32] Maddox, S. J., et al. 1990, MNRAS, 242, 43
- [33] Maller, A. H., et al. 2003, astro-ph/0304005
- [34] Myers, A.D., Shanks, T. Outram, P.J., Wolfendale, A.W. 2003, astro-ph/0306180
- [35] Nikolaev, S., et al. 2000, AJ, 120, 3340
- [36] Nolta, M.R., et al. 2003, astro-ph/030597
- [37] Peacock, J.A., & Dodds, S.J. 1996, MNRAS, 280L, 19
- [38] Peebles, P. J. E., & Ratra, B. 2003, Rev.Mod.Phys. 75, 599
- [39] Peiris, H., & Spergel, D.N. 2000, ApJ, 540, 605
- [40] Refregier A., Komatsu E., Spergel D. N., Pen U., 2000, Phys. Rev. D, 61,123001
- [41] Sachs, R. K. & Wolfe, A. M. 1967, ApJ, 147, 73
- [42] Schechter, P. 1976, ApJ 203, 296.
- [43] Schlegel, D.J., Finkbeiner, D.P. & Davis, M. 1998, ApJ 500, 525.
- [44] Scranton, R. et al. 2003, astro-ph/0305337

- [45] Seljak, U. & Zaldarriaga, M. 1996, ApJ, 469, 437
- [46] Sheth, R. K. & Tormen, G. 1999, MNRAS, 308, 119
- [47] Spergel, D.N. *et al.* 2003, astro-ph/0302209.
- [48] Skrutskie et al. 1997, in *The Impact of Large Scale Near-IR Sky Survey*, ed. F. Garzon et al. (Dordrecht: Kluwer), 187
- [49] Tegmark, M. 1997, Phys. Rev. D, 56, 4514
- [50] York, D.G. *et al.* 2000, AJ, 120, 1579
- [51] Zel'dovich Y.B., & Sunyaev, R.A. 1967, ApSpSci, 4, 301.
- [52] We thank Doug Finkbeiner for extracting the fluxes of Andromeda in WMAP temperature maps.
- [53] We thank Eiichiro Komatsu for pointing out this identity.
- [54] This is different from  $R_K = 0.35$  used by [28] whose luminosity function parameters we use to estimate the redshift distribution, but the median difference of extinction derived between the two is small(< 0.002 mag).
- [55] This is also the level chosen by [33] for their auto-correlation analysis of the XSC.
- [56] Given that the galaxy distribution is non-linear and non-gaussian, the  $\chi^2$  fit is not the optimal bias estimator. However, the fact that the biases for different bins are so close implies that the error in bias, as we see below, is much smaller than the error in our cross-correlation signal and so is negligible.

## APPENDIX A: SEMI-ANALYTICAL ESTIMATE OF SZ SIGNAL

In order to find  $\tilde{T}_e$  (defined in Eq.7) we need an expression for the dependence of the electron pressure overdensity on the matter overdensity. As the shock-heated gas in clusters of galaxies has keV scale temperatures and constitutes about 5 – 10% of the baryonic mass of the universe, its contribution to the average pressure of the universe is significantly higher than the photo-ionized inter-galactic medium (at temperatures of a few eV). Thus, the average electron pressure in a large region of space with average density  $\bar{\rho}(1 + \delta_m)$  is given

by

$$\begin{aligned}\delta p_e &\simeq \frac{\bar{n}_e}{\bar{\rho}} \int dM \cdot M \cdot k_B [T_e(M; \bar{\rho}) \frac{\partial n(M; \bar{\rho})}{\partial \bar{\rho}} + n(M; \bar{\rho}) \frac{\partial T_e(M; \bar{\rho})}{\partial \bar{\rho}}] \bar{\rho} \delta_m \\ &= \frac{\bar{n}_e}{\bar{\rho}} \int dM \cdot M \cdot n(M; \bar{\rho}) [k_B T_e(M; \bar{\rho})] [b(M) + \frac{\partial \log T_e}{\partial \log \bar{\rho}}] \delta_m,\end{aligned}\quad (\text{A1})$$

where  $n(M; \bar{\rho})$  and  $T_e(M; \bar{\rho})$  are the mass function and temperature-mass relation of galaxy clusters respectively. Also,  $b(M) = \frac{\partial \log n(M; \bar{\rho})}{\partial \log \bar{\rho}}$  is the bias factor for haloes of virial mass  $M$  ( $= M_{200}$ ; mass within the sphere with the overdensity of 200 relative to the critical density). For our analysis, we use the Sheth & Tormen analytic form [46], for  $n(M)$  and  $b(M)$ , which is optimized to fit numerical N-body simulations.

We can use theoretical works on the cluster mass-temperature relation (which assume equipartition among thermal and kinetic energies of different components in the intra-cluster medium) to find  $T_e(M)$ , (e.g. [2])

$$\begin{aligned}\frac{k_B T_e(M)}{m_p} &\simeq (0.32Q)(2\pi G H M)^{2/3} \\ \Rightarrow T_e(M) &= (6.62 \text{ keV})Q \left( \frac{M}{10^{15} h^{-1} M_\odot} \right)^{2/3}, \\ \text{while} \quad 1 < Q < 2\end{aligned}\quad (\text{A2})$$

for massive clusters, where  $H = 100h \text{ km s}^{-1}/\text{Mpc}$  is the (local) Hubble constant. Although there is controversy on the value of the normalization  $Q$  (see e.g. [30] and references therein), [2] argue that, as long as there are no significant ongoing astrophysical feed-back or cooling (i.e., as long the evolution is adiabatic), the dependence on  $H$  and  $M$  should be the same. Combining this with the local comoving continuity equation

$$3(H + \delta H) = -\frac{\dot{\bar{\rho}}}{\bar{\rho}} - \dot{\delta}_m, \quad (\text{A3})$$

yields

$$\frac{\partial \log T_e}{\partial \log \bar{\rho}} = \frac{2}{3} \frac{\partial \log H}{\partial \log \bar{\rho}} = -\frac{2\dot{D}}{9DH}, \quad (\text{A4})$$

where  $D$  is the linear growth factor.

One may think is that observations may be the most reliable way of constraining  $Q$  in Eq.(A2). However, almost all the observational signatures of the hot gas in the intra-cluster medium come from the X-ray observations which systematically choose the regions with high gas density. With this in mind, we should mention that while observations prefer a

value of  $Q$  close to 1.7, numerical simulations and analytic estimates prefer values closer to 1.2[2]. For our analysis, we treat  $Q$  as a free parameter which we constrain using our cross-correlation data (see Sec. V.A).

Putting all the pieces together, we end up with the following expression for  $\tilde{T}_e$

$$\begin{aligned}\tilde{T}_e &= (0.32 Q)(2\pi GH)^{2/3} \\ &\times \int d\nu f_{ST}[\nu] M^{2/3} [b_{ST}(\nu) - \frac{2\dot{D}}{9DH}], \\ \nu(M) &= \frac{\delta_c}{\sigma(M)}\end{aligned}\quad (A5)$$

where  $\sigma(M)$  is the variance of linear mass overdensity within a sphere that contains mass  $M$  of unperturbed density, while  $\delta_c \simeq 1.68$  is the spherical top-hot linear growth threshold[20].  $f_{ST}$  and  $b_{ST}$  are defined in [46]. For the WMAP concordance cosmological model[5], this integral can be evaluated to give

$$\tilde{T}_e = b_p \bar{T}_e = (0.88 Q) \text{ keV.} \quad (A6)$$

Finally, we comment on the scale dependence of the gas bias. Although  $b_p$  (and  $\tilde{T}_e$ ) are expected to be constant at large scales, they may vary on scales comparable or smaller than the size of clusters. This is because the gas pressure does not necessarily follow the dark matter density inside a cluster. [40] have studied the pressure bias and its scale dependence in numerical hydro-simulations of a  $\Lambda$ CDM cosmology. The result is that  $b_p$  does not significantly deviate from its large scale value for  $k < 5h \text{ Mpc}^{-1}$ . Since the average redshift of 2MASS galaxies is around  $z \sim 0.1 = H(300h^{-1} \text{ Mpc})$ , constant  $b_p$  should be a good approximation for  $\ell = kr < 1500$ , which is the case for our analysis.

## APPENDIX B: MICROWAVE LUMINOSITIES OF THE ANDROMEDA AND THE MILKY WAY

First we derive how much the flux received by a microwave source at distance  $d_L$  and observed solid angle  $\delta\Omega$  affects the observed CMB temperature. The apparent change in the black-body temperature is obtained by

$$\delta\Omega \cdot \delta \left[ \frac{4\pi(\hbar/c^2)\nu^3\Delta\nu}{\exp[\hbar\nu/(k_B T_{\text{CMB}})] - 1} \right] = \frac{L}{4\pi d_L^2}. \quad (B1)$$

The left hand side of Eq.(B1) is the change in the Planck intensity, where  $\nu$  and  $\Delta\nu$  are the detector frequency and band width respectively. The right hand side is the observed Microwave flux. Defining  $x$  as the frequency in units of  $k_B T_{\text{CMB}}/h$ , Eq.(B1) yields

$$\frac{\delta T}{T} = \frac{4\pi^2 \hbar^3 c^2}{(k_B T_{\text{CMB}})^4} \cdot \frac{\sinh^2(x/2)}{x^4 \Delta x} \cdot \frac{L}{\delta \Omega d_L^2}. \quad (\text{B2})$$

To obtain the microwave luminosity of Milky Way, we assume an optically and geometrically thin disk, with a microwave emissivity,  $\epsilon$ , which is constant across its thickness and falls as  $\epsilon_0 \exp(-r/r_0)$  with the distance,  $r$ , from its center. The disk thickness is  $2H \ll r$ , while we assume  $r_0 \simeq 5$  kpc, our distance from the Galactic center is  $r \simeq 8.5$  kpc, and our vertical distance from the center of the disk is  $z$ . Integrating Eq.(B2) over the disk thickness leads to the cosecant law for the Galactic emission

$$\frac{\delta T}{T}(b; r) = \frac{4\pi^2 \hbar^3 c^2}{(k_B T_{\text{CMB}})^4} \cdot \frac{\sinh^2(x/2)}{x^4 \Delta x} \cdot \epsilon_0 e^{-r/r_0} (H |\csc b| - z \csc b), \quad (\text{B3})$$

where  $b$  is Galactic latitude. Integrating  $\epsilon(r)$  over the disk volume gives the total luminosity of the Milky Way

$$L = 2H \int 2\pi r dr \epsilon_0 e^{-r/r_0} = 4\pi H r_0^2 \epsilon_0. \quad (\text{B4})$$

Combining Eqs.B3 and B4, we can obtain the total luminosity of Milky Way from the observed Galactic emission

$$L = r_0^2 e^{r/r_0} \cdot \frac{(k_B T_{\text{CMB}})^4}{2\pi \hbar^3 c^2} \cdot \frac{x^4 \Delta x}{\sinh^2(x/2)} \cdot |\sin b| \left[ \frac{\delta T}{T}(b; r) + \frac{\delta T}{T}(-b; r) \right]. \quad (\text{B5})$$

Figure 7 in [6] gives the cosecant law for the Galactic emission in different WMAP bands. Using this information in Eq.(B5) (after conversion into thermodynamic units) gives the luminosity of the Milky Way in WMAP bands

$$\begin{aligned} L_Q^* &= 1.7 \times 10^{37} \text{ erg s}^{-1}, \\ L_V^* &= 3.0 \times 10^{37} \text{ erg s}^{-1}, \\ \text{and } L_W^* &= 1.0 \times 10^{38} \text{ erg s}^{-1}. \end{aligned} \quad (\text{B6})$$

To confirm these values, we can use Eq.(B2) and the observed integrated flux of the Andromeda (M31) galaxy in the WMAP maps to obtain its microwave luminosity

$$\begin{aligned} L_{M31,Q} &= 2.1 \times 10^{37} \text{ erg s}^{-1}, \\ L_{M31,V} &= 5.3 \times 10^{37} \text{ erg s}^{-1}, \\ \text{and } L_{M31,W} &= 1.6 \times 10^{38} \text{ erg s}^{-1}. \end{aligned} \quad (\text{B7})$$

We see that these values are larger, but within 50%, of the Milky Way microwave luminosities.